Chemical Science

ROYAL SOCIETY OF CHEMISTRY

EDGE ARTICLE

View Article Online
View Journal | View Issue

Cite this: *Chem. Sci.*, 2022, **13**, 5999

All publication charges for this article have been paid for by the Royal Society of Chemistry

Received 6th January 2022
Accepted 25th April 2022

DOI: 10.1039/d2sc00082b

rsc.li/chemical-science

Supramolecular cuboctahedra with aggregation-induced emission enhancement and external binding ability†

Zhe Zhang,‡[a] Qixia Bai,‡[a] Erendra Manandhar,‡[c] Yunting Zeng,[b] Tun Wu,[a] Ming Wang,[b] Liao-Yuan Yao,[d] George R. Newkome,*[c] Pingshan Wang*[a] and Ting-Zheng Xie*[a]

Beyond the AIE (aggregation-induced emission) phenomenon in small molecules, supramolecules with AIE properties have evolved in the AIE family and accelerated the growth of supramolecular application diversity. Inspired by its mechanism, particularly the RIV (restriction of intramolecular vibrations) process, a feasible strategy of constructing an AIE-supramolecular cage based on the oxidation of sulfur atoms and coordination of metals is presented. In contrast to previous strategies that used molecular stacking to limit molecular vibrations, we achieved the desired goal using the synergistic effects of coordination-driven self-assembly and oxidation. Upon assembling with zinc ions, **S1** was endowed with a distinct AIE property compared with its ligand **L1**, while **S2** exhibited a remarkable fluorescence enhancement compared to **L2**. Also, the single cage-sized nanowire structure of supramolecules was obtained *via* directional electrostatic interactions with multiple anions and rigid-shaped cationic cages. Moreover, the adducts of zinc porphyrin and supramolecules were investigated and characterized by 2D DOSY, ESI-MS, TWIM-MS, UV-vis, and fluorescence spectroscopy. The protocol described here enriches the ongoing research on tunable fluorescence materials and paves the way towards constructing stimuli-responsive luminescent supramolecular cages.

Introduction

Since Ben Zhong Tang reported the AIE phenomenon for the first time,[1–4] aggregation-induced fluorescence (AIE), luminescent materials based on hexaphenylsilole, tetraphenylethene (TPE),[5,6] and 9,10-stilbenylanthracene[7] have been continuously explored and widely used in optoelectronics,[8] biosensors,[9,10] cellular imaging,[11,12] and other applications.[13–15] Following the advancement of the AIE effect, AIE systems have been progressively designed and synthesized, while attempts have also been made to introduce such systems into the field of supramolecules.[16–21] Coordination-driven bottom-up self-assembly provides a powerful tool for the design and construction of functional luminescent materials.[22] Attaching or inserting groups with the AIE effect into a supramolecular structure does not hinder the original non-covalent interaction force, while the supramolecular structure is endowed with good luminescence properties,[23,24] broadening its application horizon toward bioimaging, chemical detection, and other fields. In 2015 Stang and Huang reported the first AIE supramolecular coordination cage using a pyridine ligand containing a TPE group coordinated to metallic platinum and used this type of cage to detect amino acids.[25] However, the generation of the AIE phenomenon is currently limited to the introduction of groups with AIE effects in ligands or supramolecules.[26–29] Additionally, the coordination between fluorescent organic ligands with AIE properties often causes fluorescence quenching. Thus, even though many versatile supramolecular cages have been reported,[30–34] those with AIE effects are rather scarce. Therefore, the design and fabrication of fluorescence-tunable supramolecular cages with AIE properties, especially through non-AIE building blocks, are still challenging.

Herein, we report a remarkable example of using an ACQ ligand to obtain significant AIE coordination-driven supramolecular cages by synergistic spatial site resistance effects,

[a]*Institute of Environmental Research at Greater Bay Area, Key Laboratory for Water Quality and Conservation of the Pearl River Delta, Ministry of Education, Guangzhou Key Laboratory for Clean Energy and Materials, Guangzhou University, Guangzhou-510006, China. E-mail: xietingzheng@gzhu.edu.cn; chemwps@csu.edu.cn*

[b]*State Key Laboratory of Supramolecular Structure and Materials, College of Chemistry, Jilin University, Changchun, Jilin 130012, China*

[c]*Departments of Polymer Science and Chemistry, University of Akron, Akron, OH 44325-4717, USA. E-mail: newkome@uakron.edu*

[d]*MOE Key Laboratory of Cluster Science, School of Chemistry and Chemical Engineering, Beijing Institute of Technology, Beijing 102488, China*

† Electronic supplementary information (ESI) available. CCDC 2132604 and 2132525. For ESI and crystallographic data in CIF or other electronic format see https://doi.org/10.1039/d2sc00082b

‡ These authors contributed equally to this work.

which was a serendipitous finding. Two cuboctahedrally shaped supramolecular cages **S1** and **S2**, consisting of 12 ligands, 24 Zn^{2+}, and 48 counterions, were self-assembled, exhibiting a huge cavity with a diameter of about 6 nm according to the computer-assisted modeling. They were prepared by the combination of a thianthrene molecule (**L1**) or a thianthrene-9,9′,10,10′-tetraoxide (**L2**) molecule with 2.0 equiv. $Zn(NTf_2)_2$. The ligands (**L1**, **L2**) exhibited traditional ACQ features, while an obvious AIE phenomenon for the thianthrene complex (**S1**) was observed after coordination with Zn^{2+}, which could be caused by the inhibition of intramolecular vibrations by the coordination between the metal and ligand.[35] For the **S2** complex, the fluorescence exhibited no obvious change due to the fixed thianthrene bridge through oxygen atoms. Moreover, both cuboctahedral complexes could aggregate into single-molecule width nanoribbons by hierarchical self-assembly, attributed to the rigid shape effect and coulombic forces between the metal–organic cations and huge number of anions. In addition, the supramolecule could be used to combine zinc porphyrin, showing potential application prospects in single-molecular catalysis, highly sensitive fluorescent sensors, and other fields.

Results and discussion

Synthesis and characterization of supramolecular cages S1, S2

Using terpyridine monomers coordinated with transition metal ions [*i.e.*, <tpy-M^{2+}-tpy> (M = transition metal ion)] as linking units[36] and inspired by Archimedean solids, a series of Archimedean-shaped supramolecular cages, such as tetrahedra,[37–39] octahedra,[40,41] and cuboctahedra,[42] were reported. Based on a similar design principle, we report two cuboctahedral-shaped supramolecular cages **S1** and **S2**. The dihedral angles of thianthrene and tetra-oxide thianthrene moieties are about 149° and 144°, respectively, and they decrease to 125° to form a cuboctahedron during coordination with Zn^{2+}. **L1** and **L2** are prepared by the Suzuki coupling reaction of 2,3,7,8-tetrabromothianthrene and 2,3,7,8-tetrabromothianthrene-5,5,10,10-tetraoxide with 4-(2,2′:6′2′-terpyridine) phenylboronic acid (Schemes 1 and S1, ESI†). Afterward, ligand **L1** or **L2** is assembled with $Zn(NTf_2)_2$ at a precise stoichiometric ratio of 1 : 2 in $CHCl_3$/MeOH (1 : 1, v/v)

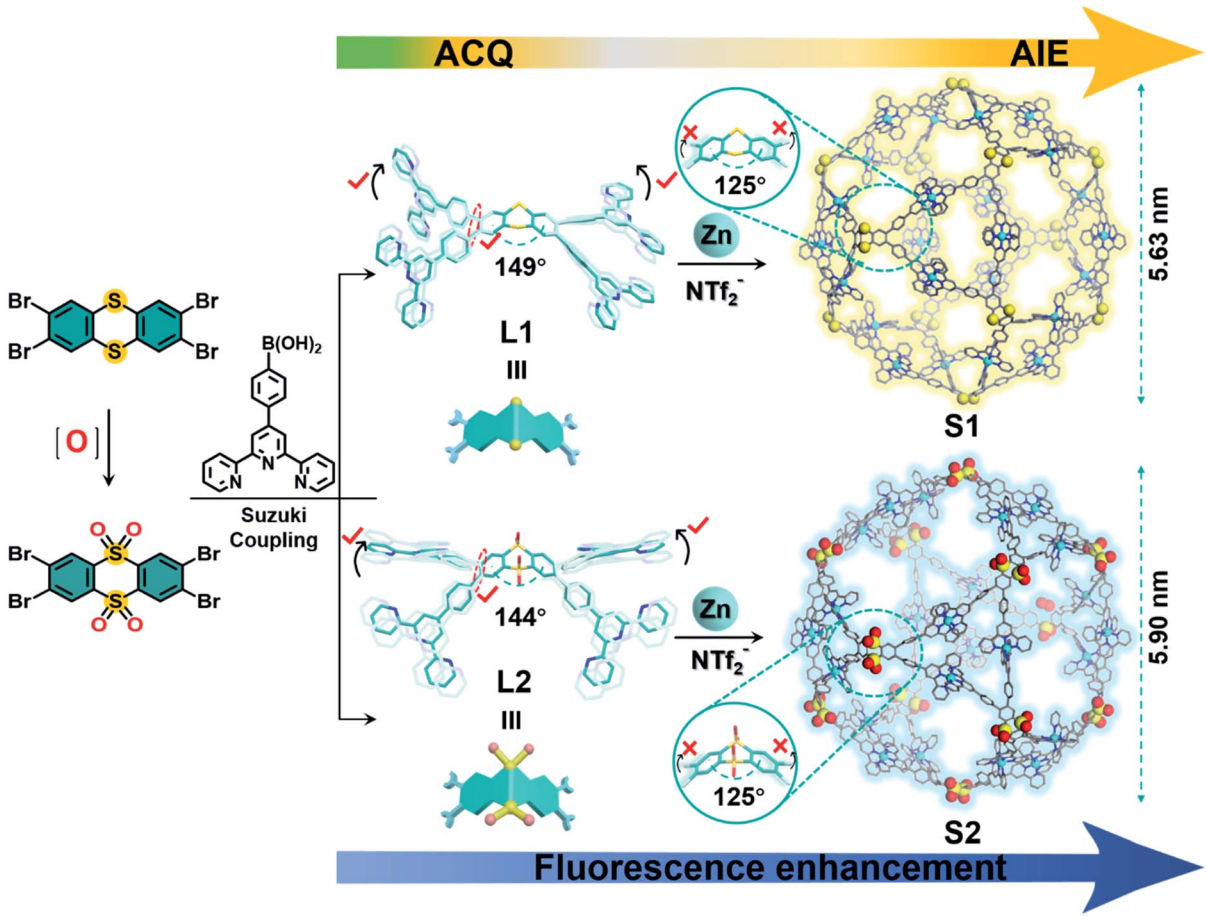

Scheme 1 Preparation of cuboctahedra **S1** and **S2** by the self-assembly of **L1**, **L2**, and Zn^{2+}. [The structures of **L1** and **L2** are the X-ray single-crystal structures (C = cyan, O = red, N = blue, S = yellow); hydrogen, and solvents were omitted for clarity; the structures of **S1**, **S2** represent optimized molecular model structures].

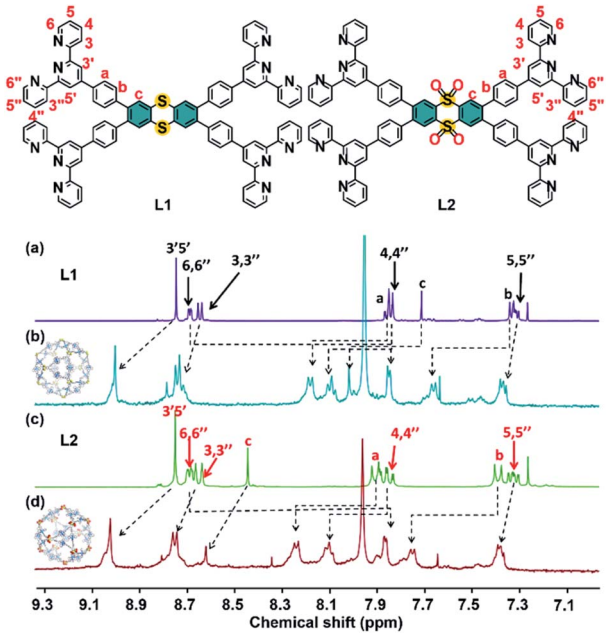

Fig. 1 ^{1}H NMR spectra (500 MHz, 298 K) of (a) **L1**, (c) **L2** in $CDCl_3$ and (b) **S1**, (d) **S2** in CD_3CN : DMF-d_7 (4 : 1, v/v).

at 55 °C for 8 h. The precipitates **S1** and **S2** are obtained by adding an excess amount of $LiNTf_2$ into the mixture and purifying it by repeated washing with deionized H_2O and MeOH. In the ^{1}H NMR spectra of **S1** and **S2**, a single set of peaks is observed, indicating the formation of a single and highly symmetric species. The signals in the ^{1}H NMR spectrum are assigned with the aid of 2D ^{1}H–^{1}H COSY and 2D ^{1}H–^{1}H NOESY NMR (Fig. S5, S6 and S10, S11, ESI†). As shown in Fig. 1, except for the signal corresponding to 6,6″-tpy hydrogen atoms, the signals of other hydrogen atoms are shifted downfield in the complexes. The upfield shift of 6,6″-tpy hydrogen atoms (from 8.68 ppm to 7.85 ppm) is indicative of the formation of the pseudo-octahedral bister pyridinyl complex moieties. Diffusion-ordered NMR spectroscopy (DOSY) provides dimensional information on **S1** and **S2**, as shown in Fig. S13 and S14.† The DOSY spectra of **S1** and **S2** show a narrow band of signals with a diffusion coefficient (D) around 9.55×10^{-11} and 8.91×10^{-11} $m^2\ s^{-1}$, indicating the presence of a single species in the solution, separately. According to the Stokes–Einstein equation, the calculated radii of the spherical complexes are 5.44 and 5.82 nm, which were fitted in with the sizes obtained by molecular modeling (5.63 nm and 5.90 nm).

Furthermore, multidimensional mass spectrometric techniques, including ESI-MS, traveling wave ion mobility mass spectrometry (TWIM-MS), and gradient tandem mass

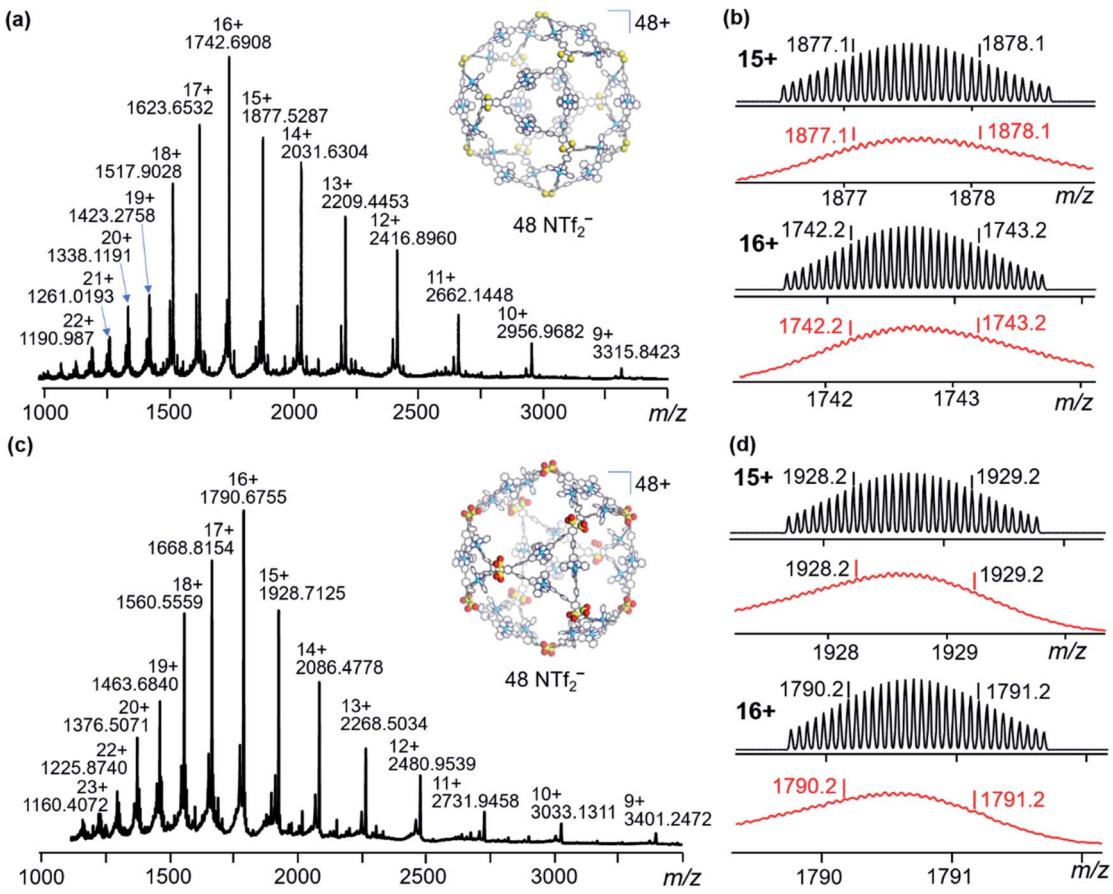

Fig. 2 ESI-MS spectra of (a) **S1** and (c) **S2**; isotopic patterns of two charge states for (b) **S1** and (d) **S2**. Top: the calculated value, bottom: the experimental value.

spectrometry (gMS^2), provide further evidence for the formation of an accepted discrete assembly. In Fig. 2a and c, the **S1** solution shows one dominant set of peaks with continuous charge states from 9+ to 22+, and **S2** shows signals ranging from 9+ to 23+. After deconvolution of *m*/*z*, the average measured molecular mass of the assembly is 32 364 Da $[(C_{96}H_{60}N_{12}S_2)_{12}Zn_{24}(C_2F_6NO_4S_2)_{48}]$ and 33 132 Da $[(C_{96}H_{60}N_{12}S_2O_4)_{12}Zn_{24}(C_2F_6NO_4S_2)_{48}]$, which agrees with the molecular composition of **S1** and **S2**. The experimental isotope patterns of each charge state (Fig. 2b and d) are consistent with the theoretical simulations. The TWIM-MS experiment separates the ions based on the size/shape and charge.[43] The TWIM-MS spectra exhibit a single band of signals with charge states of 12+ to 23+ for **S1** and charge states of 10+ to 23+ for **S2**, indicative of a single species existing in the solution for both complexes (Fig. S21, ESI†). gMS^2 experiments were performed on the 17+ ions at *m*/*z* of 1623.7 and 1668.8 by collision-induced dissociation with collision energies ranging from 4 to 43 V (Fig. S24 and S25, ESI†). **S1** dissociates at 41 V, while **S2** dissociates at 43 V, exhibiting lower stability than **S1** in the gas phase.

Transmission electron microscopy (TEM) facilitates the visualization of the cuboctahedra for **S1** and **S2**, by directly revealing both the shape and the size of individual molecules. The TEM images are obtained by depositing the DMF solutions of complexes (2×10^{-6} M) on a carbon-coated copper grid (Cu, 400 mesh), concentrating the complexes upon evaporation of the solvent before inserting the grid into the TEM under vacuum (Fig. S32 and S33, ESI†). The outlines of single molecules located on the films with edges and corners can be observed, with a diameter of 5.70 nm and 6.10 nm. Moreover, the average distance between the two edges perfectly fits the diameter of 5.63 nm and 5.90 nm which was obtained from the optimized molecular model for **S1** and **S2**. The atomic force microscopy (AFM) images of **S1** and **S2** are also obtained on freshly cleaved mica surfaces (Fig. 3b and f). According to the statistical height histogram for 100 particles from the AFM images (Fig. 3d and h), most dots have the same diameter as the theoretical predicted ones. Furthermore, Fig. 3c and g show that the observed heights of **S1** and **S2** are mostly 5.71 nm and 6.15 nm, matching the expected structures.

ACQ effects of ligands and AIE effects of supramolecules

S1 and **S2** exhibit extraordinary AIE effects, uncommon among coordination-driven supramolecules.[44,45] Firstly, **L1** shows weak emission at 550 nm in $CHCl_3$, while **L2** exhibits strong emission at 430 nm caused by the over-oxidation of the electron-donating S atom to electron-withdrawing sulphone[46,47] (Fig. S39, ESI†). Similarly, **S1** exhibits very weak yellow luminescence at 580 nm in the DMF solution, while the strongest emission peak of **S2** is blue-shifted to 450 nm. Considering the solubility and aggregation state of ligands and supramolecules, we chose the mixtures of $CHCl_3$/methanol and DMF/H_2O as good and poor solvents (Fig. S40, S43 and S44, ESI†), respectively, to perform the studies.

As depicted in Fig. 4a, when the methanol content is 10–20%, the fluorescence intensity of **L1** is enhanced with the slightly redshifted wavelength. The ligand **L1** demonstrates a typical ACQ effect (Fig. 4g), accompanied by a considerable decrease in photoluminescence intensity (Fig. 4a and c) (Φ_F < 5%) as the methanol content gradually increases. According to the single-crystal structure of **L1**, at high concentrations, there exist π–π interactions between **L1** molecules, and the excited high-energy molecules lose most of their energy through close contact thus weakening the luminescence. Furthermore, as can be seen from the CIE (Fig. 4e), the change in the **L1** fluorescence is also consistent with the one in Fig. 4g. **L2** also exhibits the same phenomenon compared with **L1**; the maximum fluorescence quantum yield is 65% at a methanol content of 50% (Fig. 4b and d), which is the best aggregation state. When the methanol content was 0–50%, **L2** shows a significant aggregation-induced emission, which contributes to the enhanced **L2** fluorescence intensity. It is attributed to the enhanced interactions between the **L2** molecules and the restricted bending and vibration of the thianthrene moiety. When the methanol content exceeds 50%, the ACQ and AIE

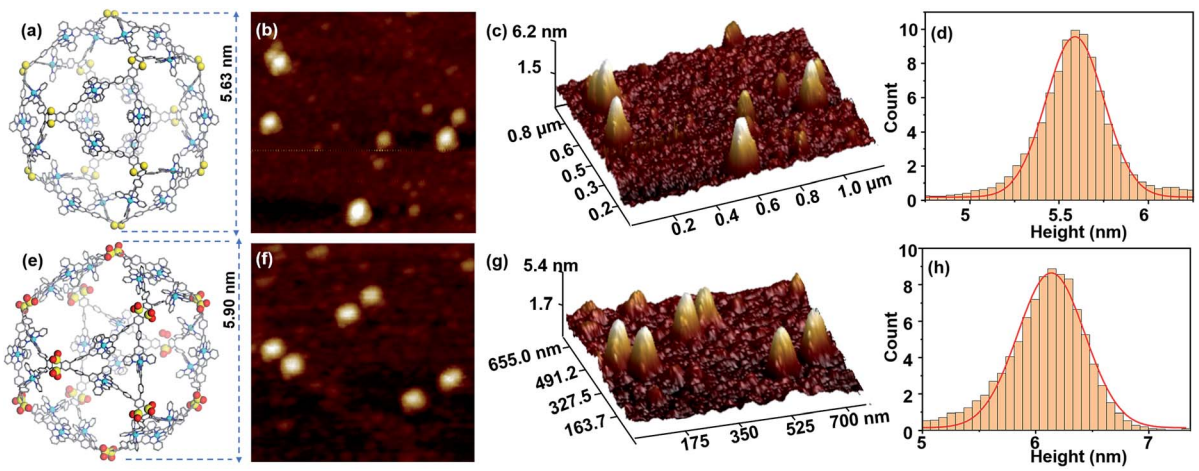

Fig. 3 AFM images of **S1** and **S2**. (a) and (e) representative energy-minimized structure from molecular modelling of **S1** and **S2**, (b) and (f) AFM images of **S1** and **S2**; (c) and (g) 3D AFM images of **S1** and **S2**; (d) and (h) height statistical histogram of AFM for 100 particles of **S1** and **S2**.

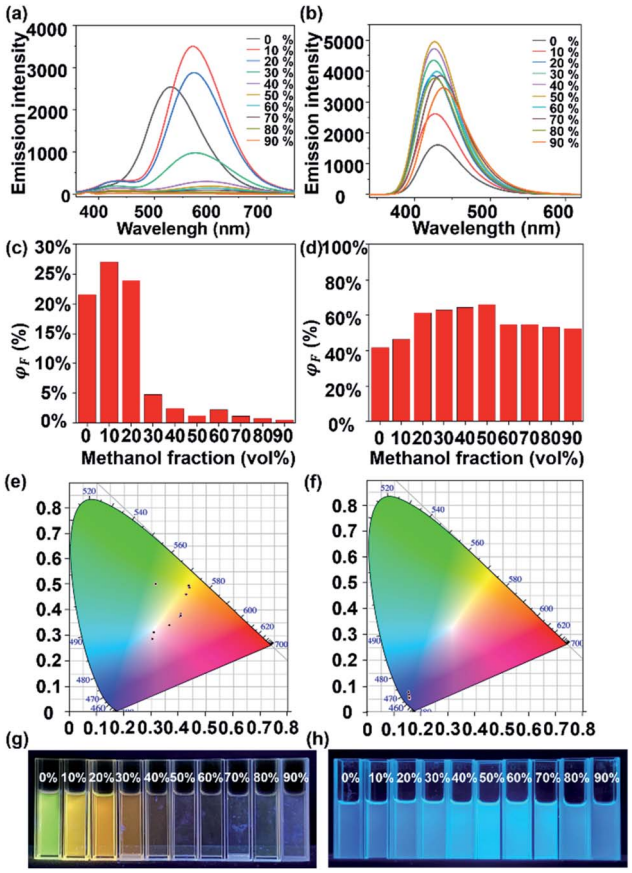

Fig. 4 ACQ of **L1** and AIE of **L2**. (a) and (b) fluorescence spectrum (λ_{ex} = 340 nm, c = 1.0 μM), (c) and (d) quantum yields, (e) and (f) CIE 1931 chromaticity diagram (the crosses signify the luminescence color coordinates), (g) and (h) photographs of **L1** and **L2** in $CHCl_3/CH_3OH$ with various methanol contents.

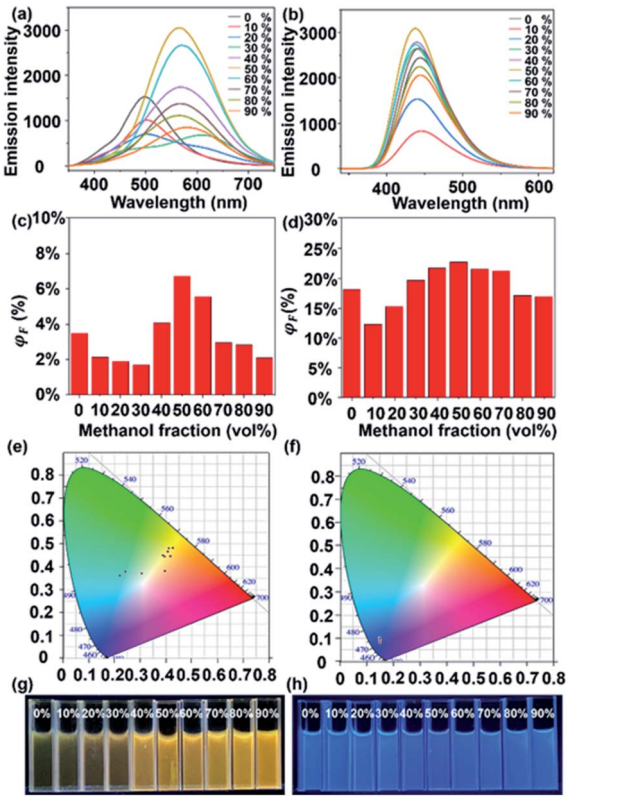

Fig. 5 AIE of **S1** and **S2**. (a) and (b) fluorescence spectrum (λ_{ex} = 340 nm, c = 1.0 μM), (c) and (d) quantum yields, (e) and (f) CIE 1931 chromaticity diagram (the crosses signify the luminescence color coordinates), (g) and (h) photographs of **S1** and **S2** in DMF/H_2O with various H_2O contents.

effects combine to reduce the overall fluorescence intensity of **L2**.[20,48] An explanation for this phenomenon is that **L2** still has the typical ACQ effect, where collisions of molecules at high concentrations lead to a partial loss of energy with increase in the undesirable solvent, resulting in the weakening of the fluorescence intensity.

In sharp contrast to **L1**, cage **S1** shows an AIE effect, which displays gradually enhanced Φ_F as the H_2O content increases, *i.e.*, from 3.7% with 0% H_2O to 7.6% with 50% H_2O (Fig. 5c). In Fig. 5a, when the H_2O content is 40%, the aggregation of **S1** reaches a certain level, and the vibrational bending of the thianthrene group is gradually limited when the AIE starts to dominate. With the H_2O content reaching 50%, the Φ_F of **S1** is 7.6%. As the H_2O proportion increases, the fluorescence intensity begins to decrease because the tight arrangement of the supramolecules increases the intramolecular collisions, which leads to energy loss. A similar phenomenon can be seen in Fig. 5e; when the H_2O content keeps increasing, the emission of **S1** mainly concentrates on the yellow light region. The TEM and dynamic light scattering (DLS) results also provide evidence for this phenomenon. From Fig. 6d–h it can be seen that **S1** aggregated into nanosphere particles in DMF/H_2O, whose size gradually increases with the H_2O content (from 5.7 nm to 61 nm). When **S1** is stacked into a nanospherical structure, the intermolecular spacing is reduced, limiting the vibration of the molecules, and leading to the appearance of the AIE phenomenon (Fig. 5g).

S2 shows an analogous phenomenon to **S1**, with a decrease in fluorescence intensity at H_2O contents of less than 30% (Fig. 5b). As the H_2O content continues to increase, the effect of supramolecular aggregation in the system becomes apparent, with the fluorescence intensity increasing until the H_2O content reaches 50% (Φ_F = 23.35%) (Fig. 5d). Another interesting phenomenon is that both **L2** and **S2** show strong blue luminescence. According to the CIE diagram (Fig. 4f and 5f), they are concentrated in the blue region of the standard color, providing a theoretical basis for further applications of supramolecular cages in light-emitting devices. Compared with the TEM results of **S1**, **S2** aggregates into much larger nanospheres when H_2O contents are 20% and 40% (about 41 nm and 49 nm, respectively, Fig. 6k and l), and intriguingly, another necklace-like aggregation appears at higher H_2O contents (Fig. 6m and n). These results agree with the higher AIE effect observed in **S2** than in **S1** (Fig. 5a and b), which also suggests that the distribution of ligands and the shape of the structural units are critical for the luminescence of the formed supramolecular structures.

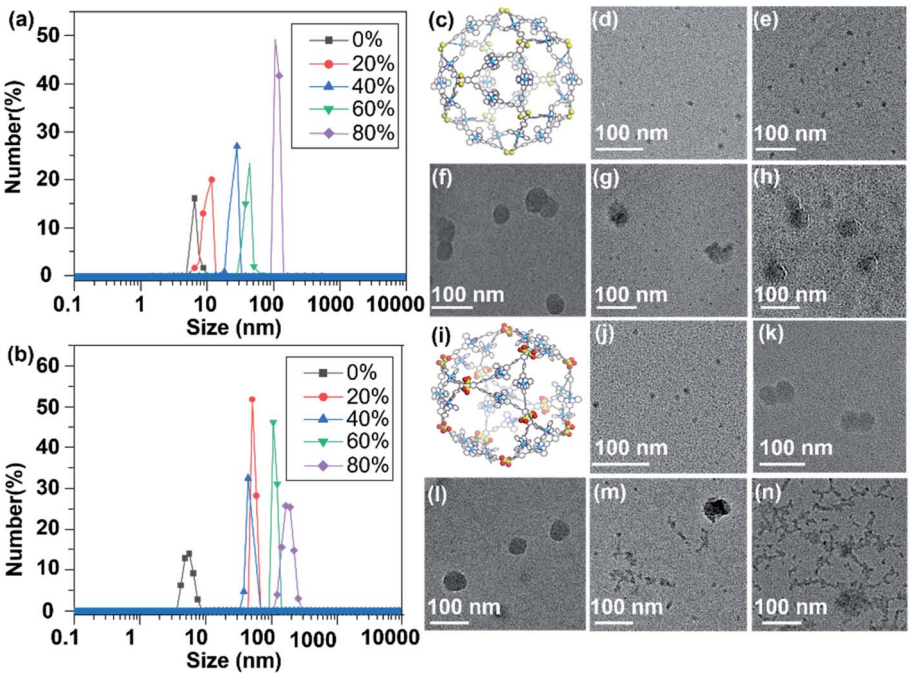

Fig. 6 TEM images and dynamic light scattering (DLS) of **S1** and **S2** aggregates. (a) and (b) size distributions of **S1** and **S2** in DMF/H_2O mixtures determined by DLS (the percentages in the graphs are the poor solvent contents); (c) and (i) representative energy-minimized structure from the molecular modeling of **S1** and **S2**. TEM images of **S1** and **S2** in DMF/H_2O mixtures containing (d) and (j) 0%, (e) and (k) 20%, (f) and (l) 40%, (g) and (m) 60%, (h) and (n) 80% H_2O.

Hierarchical self-assembly of S1 and S2

Firstly, all the samples are obtained by diffusing diethyl ether into the complex solution (2 mg mL^{-1} in DMF). Surprisingly, the one-by-one accumulation of supramolecular cages *via* directional electrostatic interactions with multiple anions and cationic cages in the fibrous structure can be clearly seen in the TEM images (Fig. 7a–c and S34, ESI†).[49] The diameters of nanotubes (4.1 nm) are consistent with the individual supramolecule **S1** from the energy-minimized structure. In our previous work, we found that cuboctahedral structures were stacked in square faces through crystal structures,[42] so it is assumed that the hierarchical self-assembly of nanofiber structures is packed in the same way (Fig. 7g). In Fig. 7d–f, the formation of fiber-like nanostructures for **S2** through the gathering of individual supramolecular structures can also be seen (Fig. S35, ESI†). In addition, according to the change process in Fig. S36,† supramolecular **S2** first aggregates to form a nanofibrous structure, then a distinct strip-like structure with further diffusion of diethyl ether, finally aggregating into a sphere. We performed elemental analysis tests on these two parts to demonstrate that the spherical and necklace-like structures were also agglomerated from **S2** (Fig. S37 and S38, ESI†). The results show that these two parts contain the same elements as **S2** and approximately the same elemental proportions, also providing evidence for our speculation on the formation process of the spherical structure.

Interaction between supramolecular structures and zinc porphyrin

Herein, the initial study using trimethoxy-porphyrin as the guest was conducted. According to the analysis, porphyrins more likely coordinate with the zinc of supramolecules, disrupting the supramolecular structure (Fig. S26, ESI†). Consequently, zinc porphyrins are used for further investigation. We

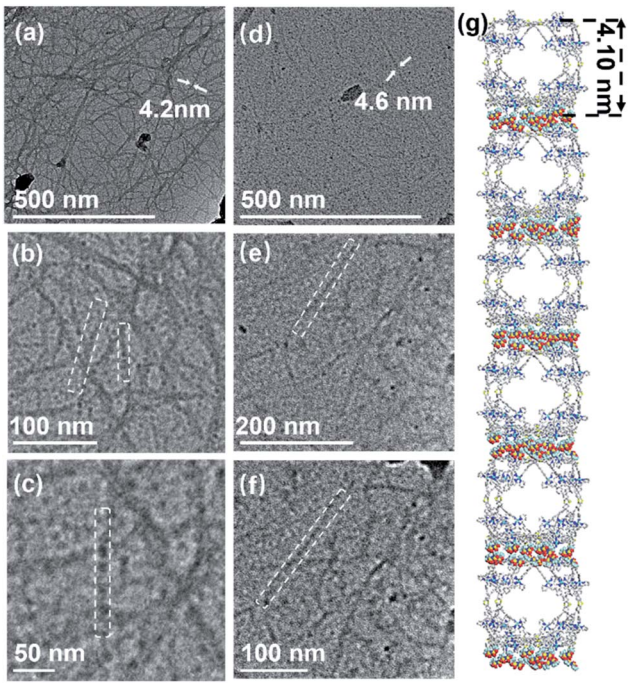

Fig. 7 Stepwise zoom of the TEM image in the same area of nanofibers assembled by S1 (a–c) and S2 (d–f) (2 mg mL^{-1} in the DMF solution under ethyl ether vapor) and (g) the probable stacking approaches of **S1** (stacking with square surfaces as contact surfaces).

performed the test by dropwise adding the guest molecule (6.0 eq.) dissolved in DMF to the supramolecular solution. The prepared complexes are confirmed by 2D DOSY, ESI-MS, TWIM-MS, gMS^2, UV-vis, and fluorescence spectroscopies. Firstly, the DOSY pattern exhibits two narrow signal bands attributed to **S1** and zinc porphyrin, indicating the external association due to the weak interactions (Fig. S19, ESI†).[50] Three sets of signals belong to free **S2** (black), one porphyrin adduct **S2**⊃**G** (green), and two porphyrin adducts **S2**⊃$\mathbf{G_2}$ (yellow), respectively, with continuous charge states from 11+ to 21+, in Fig. 8b, consistent with the TWIM-MS spectrum (Fig. 8c). These porphyrin adducts of **S2** exhibit unstable and rapid recombination behavior. Once an external voltage is imposed, the porphyrin molecules are slowly released, and when the voltage reaches 30 V, they are completely released, leaving only the cage complex (Fig. 8d). Moreover, as soon as the porphyrin solution is added dropwise, the combination of **S2** is achieved, showing no significant change with time (Fig. S30 and S31, ESI†). The applied UV and fluorescence tests on the complexes have also been used to characterize the complexes (Fig. 8e and f). Similar behavior of **S1** is further verified by DOSY, ESI-MS, TWIM-MS UV-vis, and fluorescence tests (Fig. S20, S27, S28, S46 and S47, ESI†).

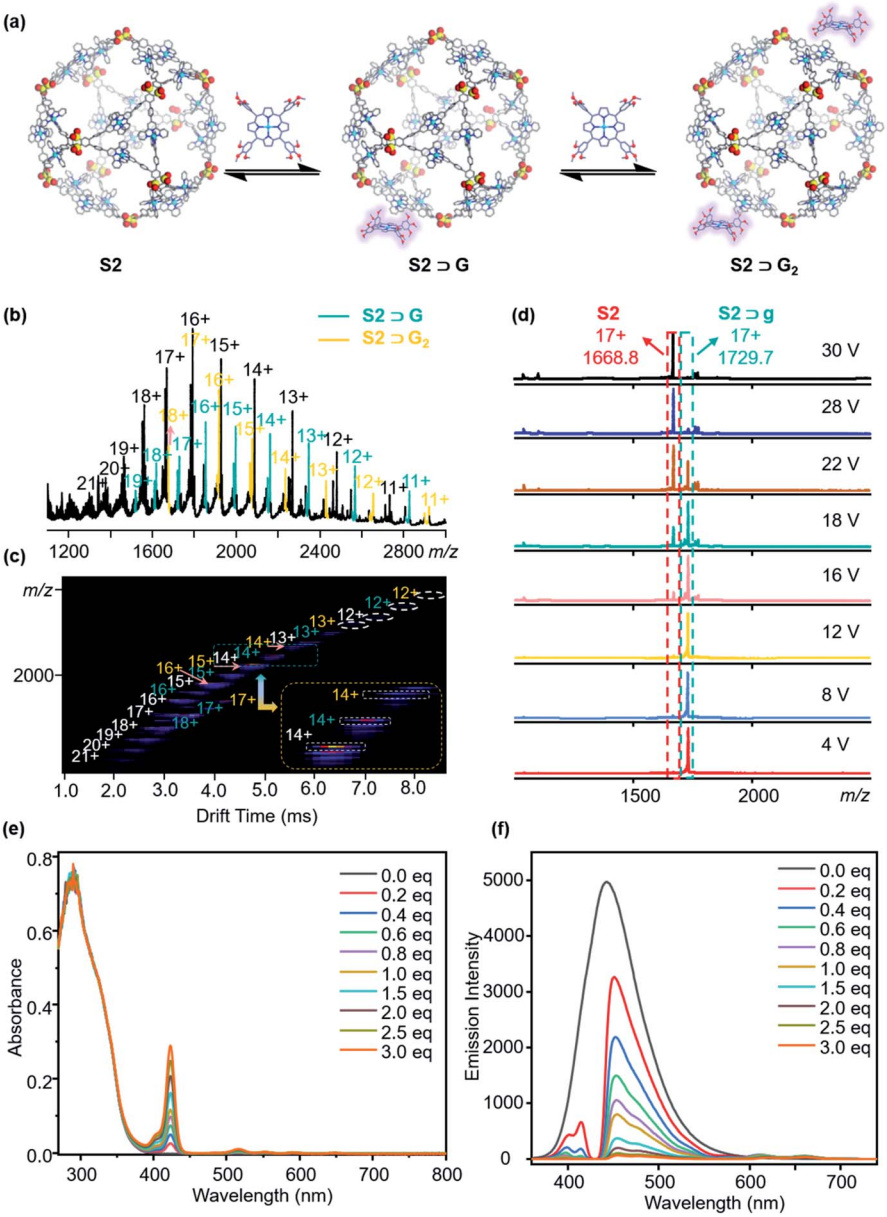

Fig. 8 (a) External combination of zinc porphyrin with **S2**; (b) and (c) ESI-MS and TWIM-MS of free **S2** (black), one porphyrin adduct **S2**⊃**G** (green), two porphyrin adducts **S2**⊃$\mathbf{G_2}$ (yellow); (d) gMS^2 of **S2**⊃**G** (NTf_2^-) at *m*/*z* 1729.7 with different collision energies; (e) UV-vis spectrum of **S2** combining different equivalents of zinc porphyrin (c = 0.5 μM); (f) fluorescence spectrum of **S2** combining different equivalents of zinc porphyrin (λ_{ex} = 340 nm, c = 1.0 μM).

Conclusions

A novel design strategy of cuboctahedral-shaped AIE-supramolecular materials has been stumbled upon, providing a novel insight into the design and synthesis of new AIE molecules. The coordination bonds served as the distal inhibition, while the oxygens around sulfur atoms introduced by oxidation served as the proximal inhibition in the atomic clip shape, severely restricting the vibration of thianthrene. Using this protocol, two AIE-supramolecular cages were constructed and characterized by NMR and TWIM-MS, and the related tunable fluorescence properties were studied by fluorescence spectrophotometry, TEM and DLS. Both **S1** and **S2** showed an optimum AIE state in an aggregated concentration at 50%. To gain a deeper insight, we prepared one-by-one stacked nanofiber structures **S1** and **S2**. In addition, the formation of an adduct between supramolecular cages and zinc porphyrins was explored in detail, providing new directions for investigating external or internal interactions between a giant cage and small molecules. Hence, we present new findings for fabricating fluorescent metal cuboctahedra with potential applications in sensing, host chemistry, and tunable luminescent materials.

Data availability

All data, models, and code generated or used during the study appear in the submitted article.

Author contributions

All authors have given approval to the final version of the manuscript. T. X. and Z. Z designed the experiments; Q. B. and Erendra Manandhar completed the synthesis; T. W. carried out the NMR analysis; Q. B. and Z. Z. did the ESI-MS test and data curation; Q. B., Z. Z. and Erendra Manandhar analyzed the experimental data. M. W. and Y. Z. did the fluorescence quantum yield tests; Q. B. and Z. Z. wrote the manuscript. Z. Z., T. X., P. W. and Newkome G. R. edited the manuscript. All the authors discussed the results and commented on and proofread the manuscript.

Conflicts of interest

There are no conflicts to declare.

Acknowledgements

This research was supported by the National Natural Science Foundation of China (21971257 to P. W., 21971048 for T-Z. X and 22101061 to Z. Z.), the Guangdong Natural Science Foundation (2019A1515011358 to Z. Z.), and the Science and Technology Research Project of Guangzhou (202002030257 to Z. Z.). The authors are thankful for the TEM test and the assistance during data collection by the Modern Analysis and Testing Center of Guangzhou University. The authors thank Prof. Baohua Zhang for quantum yield tests. The authors would like to express their gratitude to EditSprings (**https://www.editsprings.cn**) for the expert linguistic services provided.

Notes and references

1 Y. Hong, J. W. Y. Lam and B. Z. Tang, *Chem. Commun.*, 2009, **29**, 4332–4353.
2 Y. Hong, J. W. Y. Lam and B. Z. Tang, *Chem. Soc. Rev.*, 2011, **40**, 5361–5388.
3 J. Luo, Z. Xie, J. W. Y. Lam, L. Cheng, H. Chen, C. Qiu, H. S. Kwok, X. Zhan, Y. Liu, D. Zhu and B. Z. Tang, *Chem. Commun.*, 2001, **18**, 1740–1741.
4 J. Mei, N. L. C. Leung, R. T. K. Kwok, J. W. Y. Lam and B. Z. Tang, *Chem. Rev.*, 2015, **115**, 11718–11940.
5 N. B. Shustova, B. D. McCarthy and M. Dincă, *J. Am. Chem. Soc.*, 2011, **133**, 20126–20129.
6 (*a*) M. Wang, Y.-R. Zheng, K. Ghosh and P. J. Stang, *J. Am. Chem. Soc.*, 2010, **132**, 6282–6283; (*b*) C. Gui, E. Zhao, R. T. K. Kwok, A. C. S. Leung, J. W. Y. Lam, M. Jiang, H. Deng, Y. Cai, W. Zhang, H. Su and B. Z. Tang, *Chem. Sci.*, 2017, **8**, 1822–1830.
7 (*a*) M. Liu, S. Onchaiya, L. Y. F. Tan, M. A. Haghighatbin, T. Luu, T. C. Owyong, R. Hushiarian, C. F. Hogan, T. A. Smith and Y. Hong, *Molecules*, 2017, **22**, 2148–2164; (*b*) X. Hu, F. Liu, X. Zhang, Z. Zhao and S. Liu, *Chem. Sci.*, 2020, **11**, 4779–4785.
8 H. Zhang, B. Zhang, Y. Zhang, Z. Xu, H. Wu, P.-A. Yin, Z. Wang, Z. Zhao, D. Ma and B. Z. Tang, *Adv. Funct. Mater.*, 2020, **30**, 2002323–2002332.
9 (*a*) X. Jiang, H. Gao, X. Zhang, J. Pang, Y. Li, K. Li, Y. Wu, S. Li, J. Zhu, Y. Wei and L. Jiang, *Nat. Commun.*, 2018, **9**, 3799–3807; (*b*) S. Ye, T. Tian, J. Christofferson Andrew, S. Erikson, J. Jagielski, Z. Luo, S. Kumar, C.-J. Shih, J.-C. Leroux and Y. Bao, *Sci. Adv.*, 2021, **7**, 1794–1807.
10 C. Sun, B. Li, M. Zhao, S. Wang, Z. Lei, L. Lu, H. Zhang, L. Feng, C. Dou, D. Yin, H. Xu, Y. Cheng and F. Zhang, *J. Am. Chem. Soc.*, 2019, **141**, 19221–19225.
11 M. Faisal, Y. Hong, J. Liu, Y. Yu, J. W. Y. Lam, A. Qin, P. Lu and B. Z. Tang, *Chem.– Eur. J.*, 2010, **16**, 4266–4272.
12 W.-C. Wu, C.-Y. Chen, Y. Tian, S.-H. Jang, Y. Hong, Y. Liu, R. Hu, B. Z. Tang, Y.-T. Lee, C.-T. Chen, W.-C. Chen and A. K. Y. Jen, *Adv. Funct. Mater.*, 2010, **20**, 1413–1423.
13 X. Cai and B. Liu, *Angew. Chem., Int. Ed.*, 2020, **59**, 9868–9886.
14 Z. Ning and H. Tian, *Chem. Commun.*, 2009, **37**, 5483–5495.
15 S. J. Toal, K. A. Jones, D. Magde and W. C. Trogler, *J. Am. Chem. Soc.*, 2005, **127**, 11661–11665.
16 L.-J. Chen, Y.-Y. Ren, N.-W. Wu, B. Sun, J.-Q. Ma, L. Zhang, H. Tan, M. Liu, X. Li and H.-B. Yang, *J. Am. Chem. Soc.*, 2015, **137**, 11725–11735.
17 H.-T. Feng, Y.-X. Yuan, J.-B. Xiong, Y.-S. Zheng and B. Z. Tang, *Chem. Soc. Rev.*, 2018, **47**, 7452–7476.
18 G. Li, Z. Zhou, C. Yuan, Z. Guo, Y. Liu, D. Zhao, K. Liu, J. Zhao, H. Tan and X. Yan, *Angew. Chem., Int. Ed.*, 2020, **59**, 10013–10017.
19 Y. Okazawa, K. Kondo, M. Akita and M. Yoshizawa, *J. Am. Chem. Soc.*, 2015, **137**, 98–101.

20 G.-Q. Yin, H. Wang, X.-Q. Wang, B. Song, L.-J. Chen, L. Wang, X.-Q. Hao, H.-B. Yang and X. Li, *Nat. Commun.*, 2018, **9**, 567–575.
21 Z. Zhang, Z. Zhao, Y. Hou, H. Wang, X. Li, G. He and M. Zhang, *Angew. Chem., Int. Ed.*, 2019, **58**, 8862–8866.
22 P. P. Neelakandan, A. Jiménez and J. R. Nitschke, *Chem. Sci.*, 2014, **5**, 908–915.
23 D. Liu, M. Chen, K. Li, Z. Li, J. Huang, J. Wang, Z. Jiang, Z. Zhang, T. Xie, G. R. Newkome and P. Wang, *J. Am. Chem. Soc.*, 2020, **142**, 7987–7994.
24 N. Song, Z. Zhang, P. Liu, Y.-W. Yang, L. Wang, D. Wang and B. Z. Tang, *Adv. Mater.*, 2020, **32**, 2004208–2004234.
25 X. Yan, T. R. Cook, P. Wang, F. Huang and P. J. Stang, *Nat. Chem.*, 2015, **7**, 342–348.
26 W.-J. Li, X.-Q. Wang, D.-Y. Zhang, Y.-X. Hu, W.-T. Xu, L. Xu, W. Wang and H.-B. Yang, *Angew. Chem., Int. Ed.*, 2021, **60**, 18761–18768.
27 J. Mei, Y. Hong, J. W. Y. Lam, A. Qin, Y. Tang and B. Z. Tang, *Adv. Mater.*, 2014, **26**, 5429–5479.
28 C. Mu, Z. Zhang, Y. Hou, H. Liu, L. Ma, X. Li, S. Ling, G. He and M. Zhang, *Angew. Chem., Int. Ed.*, 2021, **60**, 12293–12297.
29 W. Z. Yuan, P. Lu, S. Chen, J. W. Y. Lam, Z. Wang, Y. Liu, H. S. Kwok, Y. Ma and B. Z. Tang, *Adv. Mater.*, 2010, **22**, 2159–2163.
30 (*a*) M. Tominaga, K. Suzuki, M. Kawano, T. Kusukawa, T. Ozeki, S. Sakamoto, K. Yamaguchi and M. Fujita, *Angew. Chem., Int. Ed.*, 2004, **43**, 5621–5625; (*b*) D. Fujita, Y. Ueda, S. Sato, H. Yokoyama, N. Mizuno, T. Kumasaka and M. Fujita, *Chem*, 2016, **1**, 91–101.
31 A. C. Sudik, A. R. Millward, N. W. Ockwig, A. P. Côté, J. Kim and O. M. Yaghi, *J. Am. Chem. Soc.*, 2005, **127**, 7110–7118.
32 (*a*) M. Pan, W.-M. Liao, S.-Y. Yin, S.-S. Sun and C.-Y. Su, *Chem. Rev.*, 2018, **118**, 8889–8935; (*b*) R. A. Bilbeisi, T. K. Ronson and J. R. Nitschke, *Angew. Chem., Int. Ed.*, 2013, **52**, 9027–9030.
33 J. Koo, I. Kim, Y. Kim, D. Cho, I.-C. Hwang, R. D. Mukhopadhyay, H. Song, Y. H. Ko, A. Dhamija, H. Lee, W. Hwang, S. Kim, M.-H. Baik and K. Kim, *Chem*, 2020, **6**, 3374–3384.
34 K. Byrne, M. Zubair, N. Zhu, X.-P. Zhou, D. S. Fox, H. Zhang, B. Twamley, M. J. Lennox, T. Düren and W. Schmitt, *Nat. Commun.*, 2017, **8**, 15268–15276.
35 M. Pan, W.-M. Liao, S.-Y. Yin, S.-S. Sun and C.-Y. Su, *Chem. Rev.*, 2018, **118**, 8889–8935.
36 I. Eryazici, C. N. Moorefield and G. R. Newkome, *Chem. Rev.*, 2008, **108**, 1834–1895.
37 C. M. Hong, M. Morimoto, E. A. Kapustin, N. Alzakhem, R. G. Bergman, K. N. Raymond and F. D. Toste, *J. Am. Chem. Soc.*, 2018, **140**, 6591–6595.
38 M. Kaphan David, D. Levin Mark, G. Bergman Robert, N. Raymond Kenneth and F. D. Toste, *Science*, 2015, **350**, 1235–1238.
39 T.-Z. Xie, X. Wu, K. J. Endres, Z. Guo, X. Lu, J. Li, E. Manandhar, J. M. Ludlow, C. N. Moorefield, M. J. Saunders, C. Wesdemiotis and G. R. Newkome, *J. Am. Chem. Soc.*, 2017, **139**, 15652–15655.
40 T. Wu, Z. Jiang, Q. Bai, Y. Li, S. Mao, H. Yu, L. Wojtas, Z. Tang, M. Chen, Z. Zhang, T.-Z. Xie, M. Wang, X. Li and P. Wang, *Chem*, 2021, **7**, 2429–2441.
41 C. Tan, J. Jiao, Z. Li, Y. Liu, X. Han and Y. Cui, *Angew. Chem., Int. Ed.*, 2018, **57**, 2085–2090.
42 T.-Z. Xie, K. Guo, Z. Guo, W.-Y. Gao, L. Wojtas, G.-H. Ning, M. Huang, X. Lu, J.-Y. Li, S.-Y. Liao, Y.-S. Chen, C. N. Moorefield, M. J. Saunders, S. Z. D. Cheng, C. Wesdemiotis and G. R. Newkome, *Angew. Chem., Int. Ed.*, 2015, **54**, 9224–9229.
43 Y.-T. Chan, X. Li, J. Yu, G. A. Carri, C. N. Moorefield, G. R. Newkome and C. Wesdemiotis, *J. Am. Chem. Soc.*, 2011, **133**, 11967–11976.
44 Y. Hou, Z. Zhang, S. Lu, J. Yuan, Q. Zhu, W.-P. Chen, S. Ling, X. Li, Y.-Z. Zheng, K. Zhu and M. Zhang, *J. Am. Chem. Soc.*, 2020, **142**, 18763–18768.
45 F. J. Rizzuto, L. K. S. von Krbek and J. R. Nitschke, *Nat. Rev. Chem.*, 2019, **3**, 204–222.
46 M. J. Aroney, R. J. W. Le Fèvre and J. D. Saxby, *J. Chem. Soc.*, 1965, 571–575.
47 D. Casarini, C. Coluccini, L. Lunazzi and A. Mazzanti, *J. Org. Chem.*, 2006, **71**, 6248–6250.
48 M. Zhang, S. Yin, J. Zhang, Z. Zhou, L. Saha Manik, C. Lu and J. Stang Peter, *Proc. Natl. Acad. Sci. U.S.A.*, 2017, **114**, 3044–3049.
49 (*a*) E. Raee, Y. Yang and T. Liu, *Giant*, 2021, **5**, 100050–100068; (*b*) Y. Wang, Y. Sun, P. Shi, M. M. Sartin, X. Lin, P. Zhang, H. Fang, P. Peng, Z. Tian and X. Cao, *Chem. Sci.*, 2019, **10**, 8076–8082.
50 G. Wu, Y. Chen, S. Fang, L. Tong, L. Shen, C. Ge, Y. Pan, X. Shi and H. Li, *Angew. Chem., Int. Ed.*, 2021, **60**, 16594–16599.